Towards Continuous Spontaneous Localization Through a Magnetically Cooled Cantilever

Benali, Dalal

Towards Continuous Spontaneous Localization Through a Magnetically Cooled Cantilever

THESIS

submitted in partial fulfillment of the
requirements for the degree of

BACHELOR OF SCIENCE
in
PHYSICS

Author :	D. Benali
Student ID :	s2630818
Supervisor :	Prof.dr.ir. T. H. Oosterkamp
Second corrector :	Dr. W. Löffler

Leiden, The Netherlands, January 24, 2023

Towards Continuous Spontaneous Localization Through a Magnetically Cooled Cantilever

D. Benali

Huygens-Kamerlingh Onnes Laboratory, Leiden University
P.O. Box 9500, 2300 RA Leiden, The Netherlands

January 24, 2023

Abstract

The effects of the continuous spontaneous localization (CSL) collapse model can theoretically be observed through an increase of the mean energy of a collapsing system. The force noise of a magnetically cooled force sensor is used to measure its kinetic energy and improve upper bounds of certain CSL parameters, but this demands an environment with temperatures in the sub-mK regime. Measurements in this temperature range are performed with a primary flux noise thermometer and a resistance thermometer, which are subsequently compared to each other and examined for their accuracy. The result is that the two thermometers do not line up in temperature, differing in 1-2 mK at all times. Standalone, their accuracy also cannot be sufficiently ascertained. The two different sensors of the resistance thermometer have a mean temperature difference of 0.93 ± 0.07 mK due to being calibrated elsewhere, causing their RC time delay to scale differently over temperature. The noise spectra of the flux noise thermometer contain interference, which is minimized as much as possible. This procedure works better for lower frequencies than for higher frequencies and has a clear effect on the flux noise power. The reliability of this thermometer is affected by a forced best fit estimation that is caused by a limiting calibration process. Besides this, the force noise measurements could not be done because the experiment did not manage to cool down enough. The reasons for this stem from small oversights in

the experimental setup. However, given that the setup has undergone improvements since the last time these measurements were performed, one can expect to improve upper bounds in future runs. This is especially the case if the temperature can be further lowered by implementing a second magnetic cooling stage.

Contents

Chapter 1

Introduction

The inception of quantum mechanics in the twentieth century had the purpose of branching out our understanding of the physics that occurs at the smallest scales, and is therefore inherently concerned with the behaviour of (sub)atomic systems. While certain quantum effects have revealed themselves to be the origin of observable macroscopic characteristics [1], any testing concerning quantum mechanics has historically been restricted to microscopic systems [2].

Prior to testing such a system, while it has not yet been externally influenced and thus remains undisturbed, quantum mechanics postulates that the possible states of the system evolve alongside each other in time according to the Schrödinger equation. The manner of evolution is both linear, meaning that some states of the system are linear combinations of other solutions to the equation, and deterministic [3]. The latter implies that any future state can be obtained by means of multiplication of the initial state with the unitary operator. In fact, this can be generalised to one of the quantum mechanical axioms that proposes the unitarity of any time evolution of a closed system that involves the Schrödinger equation [4]. The principle of unitarity claims that at least one of the possible quantum states must be realised at all times, accomplished by imposing the condition that the probabilities of all states must add up to be 1. This condition dictates what matrix transformations are allowed in Hilbert space, and consequently, given any quantum state and the unitary matrix, restricts what future and past states are possible. In other words, it grants us the ability to obtain knowledge about the system at any time [5] as well as reverse its evolution [6].

1.1 The Measurement Problem

An evident issue with unitarity, one that makes a compelling argument for departing from this feature of time evolution, arises if we start disturbing our quantum system via measurements. The Copenhagen interpretation tells us that there is an instantaneous projection of the wave function onto an eigenstate of the measured observable. This process is entirely stochastic and therefore goes against the predictability characteristic that defines the evolution of our undisturbed system. Another glaring contradiction with the evolution before measurement is that the projection process is nonlinear [3]. These two properties of projection, or wave function collapse, form an undeniable and fundamental problem with the the formulation of standard quantum mechanics. It flags the two principles of time evolution that are at odds with each other as an indication that there is a need to reconstruct the dynamics of quantum systems in a way that is not always linear or unitary [7]. This is further reiterated by the relating macro-objectification problem, which describes the validity of macroscopic superposition states that are not actually observed in reality [8], suggesting that any proposed changes should aim to reduce these indefinite states.

1.1.1 Collapse Models

Allowing to break away from the necessity of unitarity and linearity in the dynamics of quantum systems leads us onto the path of dynamical reduction models, which modify the Schrödinger equation through the addition of a stochastic term in an attempt to unify the two different kinds of evolution [3]. The implication of this addition is that wave function collapse can occur spontaneously and randomly, even in the absence of an external influence. These so called spontaneous collapse theories rid measurements of their ambiguity through the implementation of a sound mathematical framework, while still allowing the system to evolve according to the Schrödinger equation in between those collapses [8][9]. Within these models, it's crucial that the macro-objectification problem is addressed alongside the measurement problem. This is achieved through the requirement of a process for rapid suppression of macroscopic superposition states that simultaneously leaves microscopic states unaffected, thereby defining the framework in accordance to empirical observations [9].

Of the proposed models, there is one in particular that displays the desired properties that have been laid out in a way that appears physically as the most plausible, namely the continuous spontaneous localization (CSL)

model [9][10]. It introduces a collapse rate that rises in intensity as the system is increased in size in such a way that spatially larger systems experience more collapses over a period of time. Consequently, macroscopic systems can be perceived as continuously collapsing while standard quantum mechanics remains applicable to conventional microscopic systems. Another important parameter is the correlation length, which describes the spatial resolution of the collapse [11].

An exciting aspect of CSL is that it allows for experimenting on systems that are not necessarily microscopic and to test the validity of the idea of a wave function collapse as a result of a measurement. The latter can be carried out due to an energy violation that is predicted by CSL in the case a collapse event. If the collapse rate of the system is high enough, the produced energy is indirectly measurable. In 2018, Vinante et al. [11] developed a method to find the upper bounds of the CSL parameters through measuring the energy of a mechanical resonator in a thermal bath. By improving upper bounds of these parameters, one could eventually make the sensible assumption that the measured energy is due to wave function collapse. However, since the violation is incredibly small, excellent vibration isolation as well as a sub-mK environment are demanded [12].

The Oosterkamp group has since built upon the CSL experiment to find the kinetic energy of a silicon cantilever through force noise measurements. It is key to maximally reduce the thermal bath temperature, reaching cryogenic temperatures while simultaneously maintaining a low standard for external mechanical noise. This thesis specifically follows Van Heck et al. [12], which managed to decrease the cantilever temperature to approximately 1 mK, by implementing an improvement upon the experimental setup to establish a similar temperature for the silicon sample that is thermally linked to the measuring device. It will also go into the techniques that are required to ascertain the validity of such temperature measurements by means of a primary magnetic flux noise thermometer.

Chapter 2

Theory

2.1 Continuous Spontaneous Localization

The CSL model is a well studied and elaborate collapse model, and therefore interesting with regard to the quantum mechanics of macroscopic systems. The resulting implication of an increased mean energy enables experimentalists to set upper bounds for the aforementioned parameters. The aim of this is to eventually detect effects of the model.

2.1.1 CSL parameters

To understand where the CSL parameters come from, we rely mostly on the mathematical framework set up in Bassi and Ghirardi [3]. The time evolution of the wave function ψ_t within the CSL model can be described through a mass-proportional version of the dynamical equation, given by

$$d\psi_t = \left[-\frac{i}{\hbar} H dt + \frac{\sqrt{\gamma}}{m_0} \int d\mathbf{x} \left(M(\mathbf{x}) - \langle M(\mathbf{x}) \rangle_t \right) dW_t(\mathbf{x}) - \frac{\gamma}{2m_0^2} \int d\mathbf{x} \left(M(\mathbf{x}) - \langle M(\mathbf{x}) \rangle_t \right)^2 dt \right] \psi_t. \tag{2.1}$$

This differential equation is both nonlinear and stochastic. H is the Hamiltonian that is present in conventional quantum mechanics. The latter two terms on the right-hand side express the spontaneous collapse events with a parameter γ, which defines the collapse strength. m_0 is the mass of a nucleon, which is taken to be the reference mass, and $W_t(\mathbf{x})$ is the noise field that is coupled to the mass-proportional system [13]. We can define the mass density operators as

$$M(\mathbf{x}) = \sum_j m_j \int d\mathbf{y} g(\mathbf{y}-\mathbf{x}) \psi_j^\dagger(\mathbf{y}) \psi_j(\mathbf{y}). \tag{2.2}$$

Here, $\psi_j^\dagger(\mathbf{y})$ and $\psi_j(\mathbf{y})$ are the creation and annihilation operators for a particle j in position $\mathbf{y}$. Together they form the collapse operators that causes rapid suppression of certain superposition states [10]. In other words, the wave function ψ_t experiences a spontaneous collapse and becomes localized around the common eigenvectors of $M(\mathbf{x})$ [3]. The mass density operators also contain a spatial correlation function,

$$g(\mathbf{x}) = \left(\frac{\alpha}{2\pi}\right)^{3/2} e^{-(\alpha/2)\mathbf{x}^2}. \tag{2.3}$$

The correlation function relates the noise variables of $W_t(\mathbf{x})$ to the mass density of the system. It has a width α with dimensions m^{-2}. By further defining a correlation length $r_C = \alpha^{-1/2}$, we get a measure for the spatial resolution of the collapse [11][14]. The other CSL parameter can also be found using Eq. 2.3 by introducing the rate, or intensity, of the collapse as

$$\lambda_{CSL} = \gamma \left(\frac{\alpha}{4\pi}\right)^{3/2} = \frac{\gamma}{\left(8\pi^{3/2} r_C^3\right)}, \tag{2.4}$$

with dimensions s^{-1}. To see how exactly the CSL parameters contribute to reduction of superposition states, we need to consider the density matrix ρ_t, which describes the physical ensemble of normalized vectors $|\psi\rangle$ of the system [3]. The interaction of the system with its environment, called quantum decoherence, causes *apparent* wave function collapse [10]. The consequence of decoherence for the density matrix is the decay of its off-diagonal elements [15]. For a single nucleon, this reduction is expressed as

$$\frac{\partial}{\partial t} \langle \mathbf{x}' | \rho_t | \mathbf{x}'' \rangle = \Gamma\left(\mathbf{x}', \mathbf{x}''\right) \langle \mathbf{x}' | \rho_t | \mathbf{x}'' \rangle, \tag{2.5}$$

with $\Gamma\left(\mathbf{x}', \mathbf{x}''\right)$ the reduction rate. In terms of the CSL parameters, it becomes

$$\Gamma\left(\mathbf{x}', \mathbf{x}''\right) = \lambda_{CSL}\left[1 - e^{-|\mathbf{x}'-\mathbf{x}''|^2/4r_C^2}\right]. \tag{2.6}$$

The reduction rate is a function for the state in which the spatially separated positions $\mathbf{x}'$ and $\mathbf{x}''$ appear simultaneously at time t. Eq. 2.6 shows that if $|\mathbf{x}' - \mathbf{x}''| << r_C$, the reduction rate shrinks to zero, meaning that there is no contribution to the collapse. However, for $|\mathbf{x}' - \mathbf{x}''| \geq r_C$, the

reduction rate is roughly equal to the collapse rate λ_{CSL}. It follows that superpositions of particles that are separated by approximately the correlation length are quickly suppressed, while smaller superposition states remain nearly unaffected. This is however only the case for a single nucleon. Applying this reduction mechanism to multi-particle systems, we get the following reduction rate:

$$\Gamma = \lambda_{CSL} n^2 N. \tag{2.7}$$

Given a dense system, n^2 denotes the number of particles that are within range of each other in terms of r_C. If a particle in the system undergoes spontaneous collapse, it induces its n neighbors to also undergo collapse, creating a multi-particle collapse event. This cluster of collapse amplifiers repeats itself N times in the system [10][15].

CSL experiments mainly focus on improving bounds for λ_{CSL} and r_C, as shown in Fig. 2.1 [11]. The λ_{CSL}, r_C-plane gives an overview of what values for the collapse rate (in the full range of r_C) can be excluded as well as the redefinitions of these parameters that have been made by various experiments.

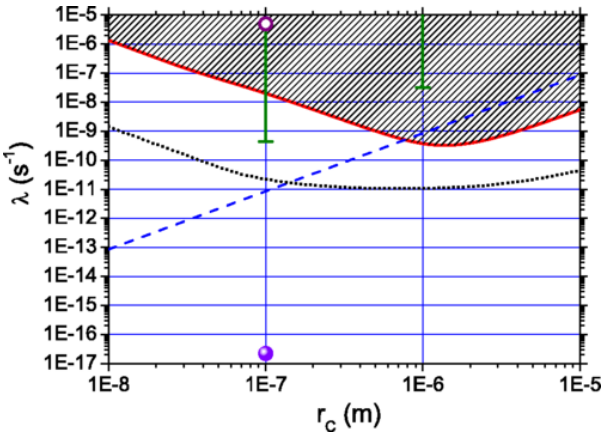

Figure 2.1: *Plot of the λ_{CSL}, r_C-plane for theoretical and experimental bounds. The shaded region above the red upper limit forms the exclusion zone of the parameters according to Vinante et al. [11]. The black dashed line is a theoretical limit that was proposed by the same group.The blue dashed line is the upper bound that is the result of an X-ray emission experiment, showing improvements from Vinante et al. at $r_C > 10^{-6}$ m [16]. The green bars are the lower bounds for two values of r_C by Adler [14]. The purple unfilled and filled dots are the upper limits of matter-wave interferometry [17][18] and proposal of the GRW-model [9].*

2.2 Noise Thermometry

An important requirement of measurements that can detect CSL effects is that they are performed at temperatures in the sub-mK regime. This is because the induced change in thermal energy results in a slight temperature change, which can only be observed if the thermal bath around collapse is at a sufficiently low temperature. The monitoring of such temperatures in this experiment is done with a primary thermometer. This type of thermometer is not calibrated with another kind of thermometer to determine temperatures, and instead directly measures thermodynamic temperature of a system. There are multiple ways of going about this, one being through noise thermometry [19].

2.2.1 Thermal Noise

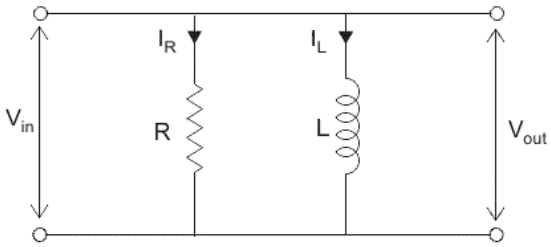

Figure 2.2: *Electrical diagram of a parallel connected resistor with resistance R (Ω) and inductor with inductance L (H). The voltage over the circuit comes from the voltage fluctuations [20].*

The method for noise thermometry relies on the thermal motion of electrons inside of a conductor that is at equilibrium. If we consider a parallel LR-circuit (see Fig. 2.2), we can use the equipartition theorem to relate the resulting thermal fluctuations to the energy stored in an inductor:

$$\left\langle \frac{1}{2} L I^2 \right\rangle = \frac{1}{2} k_B T. \tag{2.8}$$

Here L (H) is the inductance, I (A) the current, T (K) the temperature and k_B the Boltzmann constant. The thermal fluctuations of the charge carriers create a fluctuating current that runs through the resistor. According to the fluctuation-dissipation theorem, this then results in the dissipation of thermal energy. The corresponding noise is referred to as Johnson-Nyquist or thermal noise [21]. For an ideal system, the thermal noise is

almost equivalent to white noise. Therefore, the corresponding noise spectrum is supposed to be mostly constant in the frequency domain.

By further mathematically analysing Eq. 2.8, the root-mean-square (rms) thermal noise voltage over the resistor can be defined as

$$V_{\text{noise}}\,(\text{rms}) = \sqrt{4k_BTRB}, \tag{2.9}$$

where R (Ω) is the resistance and B (Hz) the bandwidth [22]. The corresponding noise power is

$$P_{noise} = k_BTB. \tag{2.10}$$

This linear relation means that by finding the noise power, the temperature can be determined relatively easily.

2.2.2 Magnetic Flux Fluctuation Thermometer

The temperature measurements in this experiment are based on a magnetic flux fluctuation thermometer, which has two important components that make it an excellent primary thermometer for extremely low temperature detection. The first component is a conductor functioning as a temperature sensor that is thermally coupled to the system. The nonzero temperature of the system will cause the electrons to move around in the conductor. Since the thermometer has to work at low temperatures, the material of the sensor has to be made of silver and welded to the silver wire. A gradiometric pickup coil that is wrapped around the sensor picks up the thermal fluctuations in the form of magnetic flux fluctuations which induces a current in the other component [23].

The second component is a DC superconducting quantum interference device, or SQUID. The SQUID consists of an electrical loop with two Josephson junctions connected in parallel. The loop is placed in close proximity to the inductor to detect its flux changes. What makes the SQUID a uniquely sensitive magnetometer is that it changes the direction of the current inside the loop with every half a magnetic flux quantum change, where a flux quantum is denoted by Φ_0 (Wb) [24]. A circuit diagram of this thermometer can be found Fig. 3.2A.

The change in current is read out by the SQUID feedback as voltage signals. Data analysis can then be used to obtain the flux noise that was picked up by the MFFT:

$$S_\Phi = 4k_BT\sigma\mu_0^2r^3G(R/\delta). \tag{2.11}$$

Here σ is the conductivity of the sensor, μ_0 the magnetic permeability, r the sensor radius and $G(R/\delta)$ a function that describes the geometry of the thermometer. As is visible from Eq. 2.11, the flux noise is linearly related to the temperature of the system. This means that the power spectral density of S_Φ becomes smaller for lower temperatures, which can be observed in Fig. 2.3.

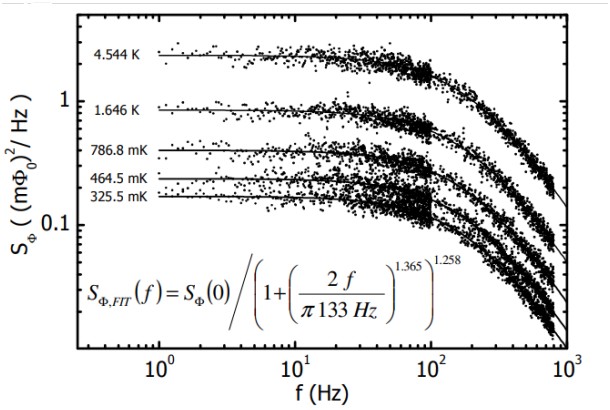

Figure 2.3: *Example of a plot of the flux noise S_Φ ($m\Phi_0^2$/Hz) over the frequency f (Hz) for multiple temperatures [19].*

Assigning one value to each spectrum, the flux noise power P_Φ can be calculated as

$$P_\Phi = \int_{f_0}^{f_1} S_\Phi df, \tag{2.12}$$

where f_0 and f_1 are the minimum and maximum frequencies of the power spectral densities respectively [12]. According to Eq. 2.10, the temperature can then be extracted from the power.

Chapter 3

Methods

3.1 Experimental Setup

The experiment, which will be referred to as Fermat, consists of a nanomechanical resonator in the form of a silicon cantilever with a permanent magnet attached to it. Acting as a force sensor in a thermal bath, it can be used to measure excess force noise that the cantilever experiences through its changing position. This displacement induces a current in a pickup loop on a diamond chip just below the cantilever. The components that make up Fermat are attached to a mass-spring system, which hangs underneath a mixing chamber plate inside a pulse-tube dilution refrigerator [25]. In Fig. 3.1, pictures of the full setup can be found. The picture on the right shows the multiple plates above the mass-spring system that together comprise the rest of the setup. The nuclear demagnetization stage (NDS) happens between the 1 K plate and the 50 mK plate (still plate). As can be seen in the left, Fermat is surrounded by an aluminium shield for protection against outside magnetic fields.

The setup is surrounded by two vacuum sealed environments: The outer vacuum chamber (OVC) and inner vacuum chamber (IVC). Starting at the room temperature plate, a pulse-tube refrigerator is used to precool the 50 K and 4 K plates, with contact gas being used for thermalization. This brings the temperature down to approximately 4 K. At this stage, helium-3 and helium-4 are brought into contact with each other in the mixing chamber. This is a cooling technique that decreases the temperature of the environment to 10-15 mK. Since the cantilever is thermally driven, we want to reduce thermal fluctuations as much as possible. To do this, the temperature is further lowered to $\lesssim 1$ mK with the NDS, which is thermally coupled to the cantilever and diamond chip through a silver wire.

The silver wire is connected to the mass-spring system in multiple places with LEGO blocks. This is so that the wire experiences vibration isolation while maintaining its temperature.

The material used inside the NDS is $PrNi_5$, and the strength of the magnet is 2 T. The contact between the mixing chamber plate and nuclear stage is controlled with an aluminium heat conductance switch. This is done by sending a current of 150 mA through a superconducting NbTi twisted pair wire that goes through both the OVC and IVC and ends up at the mixing chamber plate. The wire is thermalized to the 50 K plate and the 4 K plate. The main panel of Fig. 3.2 shows a schematic drawing of the NDS, vibration isolation system and Fermat. It also shows the two types of thermometers that are used to determine the lowest temperatures of the setup.

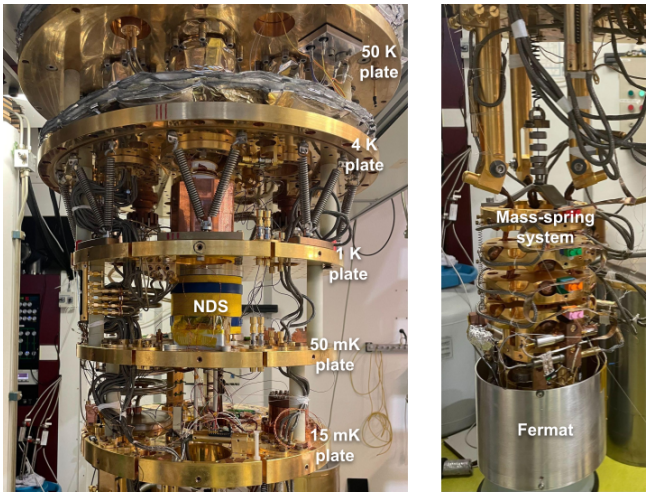

Figure 3.1: *Two pictures that show the experimental setup in its entirety. The left picture gives an overview of the temperature of each plate. These temperatures are determined with thermometers that are present on each plate. The 4* K *plate marks the transition between the OVC and IVC. In order to reduce mechanical noise, springs have been installed in between the 4 and 1* K *plates. The plates are thermally isolated from each other, so that contact gas is needed for thermalization. The right side shows the mass-spring system that hangs underneath the 15* mK *plate and Fermat with the shield below that.*

3.1.1 Fermat

As mentioned before, Fermat contains two essential components: The force sensor and the sample. The first one is an IBM-style silicon cantilever of 196 μm that has a $Nd_2Fe_{14}B$ magnet of approximately 7.3 μm in diameter

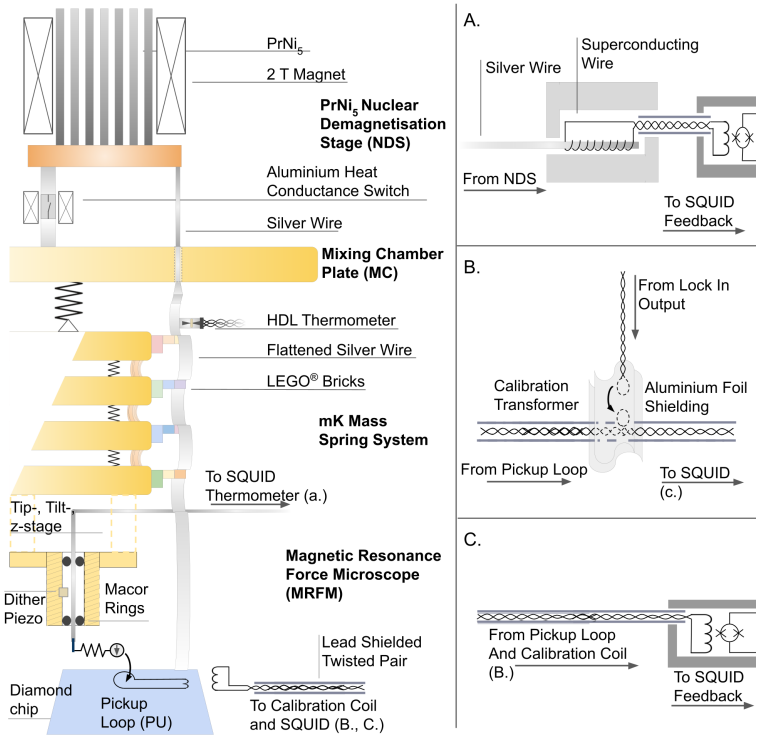

Figure 3.2: Main panel: *schematic drawing of a part of the experimental setup. The NDS is connected to the mixing stage through a heat switch. Below the mixing chamber plate, the silver wire goes through the mass-spring system and is connected to both the chip and the force sensor. There are also two types of thermometers that monitor the cantilever temperature.* Side panels: *More detailed drawings of the primary magnetic flux thermometer and cantilever readouts, which are done with SQUIDs.*

attached to the tip. The cantilever is put in a tip-holder that is connected to a dither piezo. This way, the sensor can be driven at a specific frequency. The tip-holder also has three piezoelectric motors attached to it, so that it can be titled in multiple directions. This is done so that the position of the magnet with respect to the pickup loop below can be changed to find the best coupling.

Details of how the signals from the pickup loop are transported to the SQUID feedback are shown Fig. 3.2B and C. The movement of the magnet is detected by the change of the magnetic flux in a pickup loop on a diamond chip. This induces a current that is transferred to a transformer through aluminium wire bonds. After the signal is amplified, it's lead to a SQUID where it is read out as a voltage signal. The diamond chip is thermalized to the same silver wire as the cantilever. This is done by gluing the silver wire underneath the chip with silver paint. The components

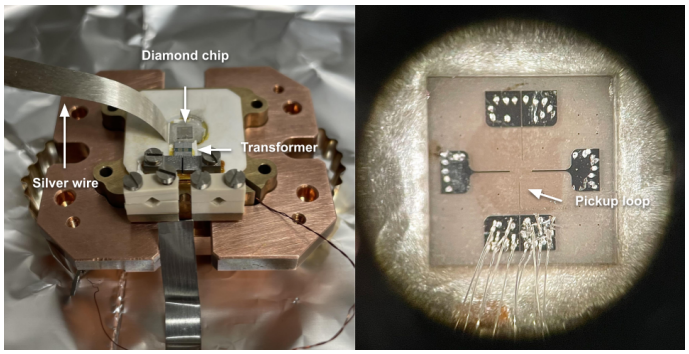

Figure 3.3: *The left side shows a picture of the sample containing the diamond chip and transformer. The silver wire is a flat so that it can be easily glued underneath the chip. The right side is a zoom-in of the diamond chip. The side with the pickup loop, which has a square shape for flux change measurements, is connected to the transformer through multiple silver wire bonds.*

below the cantilever form the sample (see Fig. 3.3).

3.1.2 Thermometers

There are two types of thermometers that are used to measure the temperatures achieved by the NDS. The first one is the magnetic flux fluctuation thermometer with a Magnicon DC SQUID, which is described in detail in section 2.2. The mechanism of the thermometer also shown in Fig. 3.2A. The temperature sensor is the silver wire that is thermally coupled to cantilever and the sample, so that the thermodynamic temperature of these components can be measured directly [26].

The second thermometer is a HDL resistance thermometer, which was developed by W. A. Bosch [12] and calibrated in another cryostat to optimally work at temperatures between 20 mK and 4 K. Since the experiment is cooled down to even lower temperatures, it is not possible to fully rely on this thermometer, and explains the necessity of a primary thermometer.

3.1.3 Setup Changes

The data that was used for the analyses of the thermometers was obtained in measurement run 58. Run 60 was carried out with the intention of doing cantilever position measurements.

Between run 56 [12] and run 58 there there was only one relevant setup change: The exclusion of Fermat in the latter run. This is because the run was meant as a test of how well the thermometers work without the effect

of the experiment. Consequently, the cables that are usually connected to Fermat did not yield a heat load that could affect the temperature of the silver wire. This also means that there was less electronic interference than if the cables would have been connected.

There were multiple setup changes between run 58 and run 60, all with the aim of improving results. The first is the removal of a set of low Ohmic cables that are generally used for the piezo motors. The cables were thermalized to the 4 K plate, but due to their heat load it is likely that they caused the plate to remain approximately 1 K above its intended temperature in previous runs.

The second change is the way in which the heat switch is connected to the power supply above the room temperature plate. A superconducting wire of NbTi inside copper with an insulating layer around it was made to replace the previous connection. Specifically, it is a twisted pair wire, where two conductors are twisted around each other in order to reduce cross talk. The wire goes down through the room temperature plate, 50 K plate and 4 K plate, being thermalized to the latter two. A vacuum tight seal was made in the 4 K plate to prevent a leak between the OVC and IVC. The resistance of full wiring of the heat conductance switch is 6.5 Ω when the fridge is in operation. The wire length was chosen in such a way that the dissipated power as a result of 150 mA of current running through it does not cause the environment in between plates to heat up. The addition of the twisted pair wire allows for a low Ohmic connection that does not cause any significant heat leakage.

A final important change is the thermalization of the diamond chip to the silver wire in order prevent the spins in the chip from heating up the cantilever. The expected effect of this is that the thermal bath temperature around the cantilever can be lowered in such a way that upper bound for CSL parameters might be improved.

3.2 Resistance Thermometer Data Analysis

The data analysis in this thesis is largely based on the previous work of B. Van Heck [12], who performed similar analyses for run 56, but has been modified for this thesis to fit the data from run 58.

During this run, four temperature sensors of the HDL resistance thermometer each measured a voltage value every 5 s between the 25th of August and 2nd of September 2022, for a total period of approximately 150 hours. In this time, a total of 135,825 usable measurements were saved to CSV files with their respective date and time of measurement and time

that has elapsed since the first measurement.

The subsequent data analysis is done using Python. The first step is to load in the files and convert the voltage to temperature values. The calibration method is specific to each temperature sensor, and the sensors that are in this case used are called the M and L sensors. The calibration implements condition based coefficients that are applied in an exponential conversion function, with a low bias correction for voltages under a certain value. Through this method, the sensor temperatures can be calculated.

Before these values can be plotted, there is a time jump in between measurements that is most likely caused by measurement equipment failing for a brief period of time. The time jump is removed by modifying the elapsed time after the jump. Plotting the temperatures

During measurements, the temperature would remain approximately the same for certain periods of time. Of course, there are temperature fluctuations in these parts of the data, for which the standard deviation can be calculated to formulate an error for the temperature,

$$\sigma_T = \sqrt{\frac{1}{(N-1)} \sum_{i=1}^{N} (T_i - \langle T \rangle)^2} \tag{3.1}$$

Here, $\langle T \rangle$ is the mean of N temperatures T_i in between sweeps.

3.2.1 RC Time

The temperature sweeps of the two sensors in Fig. 4.1 show a decrease in T that has the form of an exponential decay, characterized by the differential equation

$$\frac{dT}{dt} = -\frac{1}{\tau} T, \tag{3.2}$$

where τ (s) is the time constant. τ can also be defined as a measure of the voltage response of an RC circuit (see Fig. 3.4), and is in this case referred to as the RC time delay. Specifically, it is the time it takes to charge the capacitor to 63% of the voltage [27]. The RC time is given by $\tau = RC$, where R (Ω) is the resistance and C (F) the capacitance. We can make an analogy between τ resulting from an electrical circuit and τ resulting from the heat flow $\dot{Q}$ through a conductor. In this case, the time delay can be defined as the multiplication of the thermal resistance R_{th} (K/W) and heat capacity C_{th} (J/K). From the units it is clear that both are dependent on the temperature. The thermal resistance is calculated using

Version of January 24, 2023– Created January 24, 2023 - 22:30

$$R_{th} = \frac{L}{\kappa A}. \tag{3.3}$$

L (m) is the length of the conductor, in this case the silver wire, and A (m^2) is the area of the cross section. The thermal conductivity κ ($Wm^{-1}K^{-1}$) is found by extrapolating an existing figure using the relation $\kappa \sim T$ [28]. The heat capacity is given by

$$C_{th} = C_p M, \tag{3.4}$$

with C_p ($Jmol^{-1}K^{-1}$) the heat capacity and M ($gmol^{-1}$) the molar mass. C_p is determined in the same way as κ, where $C_p \sim T$, but through a different figure [29].

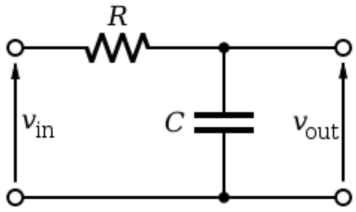

Figure 3.4: *Electrical diagram of a series RC circuit with input voltage V_{in} and output voltage V_{out}. The resistor has a resistance R and the capacitor has capacitance C [30].*

The time constant can be extracted from the exponential decay curves in Fig. 4.1 by curve fitting. The function that is used for this is the solution to Eq. 3.2, which is given by

$$T(t) = T_0 e^{-t/\tau}, \tag{3.5}$$

where T_0 (mK) is an initial temperature. The data points that mark the boundaries of the exponential decay curves are estimated by zooming in on Fig. 4.1. Since it can't actually be assumed that M and L sensor have the same decay rates, the curve fits are applied to both sensors. Two plots of the best fit estimation of one of the sweeps can be seen in Fig. 3.5. From the best fits, the RC time delay for each temperature sweep is estimated.

3.3 MFFT Data Analysis

The SQUID in the MFFT monitored the flux fluctuation for the same period of time as the HDL resistance thermometer. During that period, it sampled in increments of 61 s with a sample rate of 500,000 samples/s

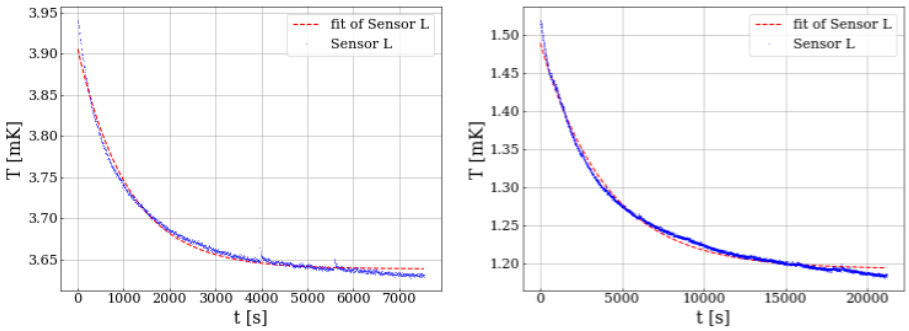

Figure 3.5: *Plot of the temperature T* (mK) *two different temperature sweeps over the time t* (s) *of the decay (blue) and the best fit estimation of the exponential decay (red).*

for a total of 3810 measurements. Before these were converted to voltage signals through a National Instruments DAQ, they were put in a SRS low-noise voltage pre-amplifier with a low-pass filter that has a higher cutoff frequency than the low-pass filter in the MFFT, the latter being a consequence of the LR behaviour of the circuit. The measurements were then digitally saved as TDMS files.

After these files are loaded into Python, they are filtered to only keep files of a specific sample size. The files that have a jump in the voltage due to SQUID failure are left out by setting a upper limit for the standard deviation of the voltage values. After this procedure, the 3357 data files that are left are coupled to the HDL resistance thermometer measurements by date and time.

In order to find the noise spectra, the power spectral density (PSD) of each measurement is calculated. This is done in the following way:

- The discrete Fourier transform (DFT) is taken. The magnitude of the result is then squared and multiplied by a sample spacing of 2×10^{-6} s. The unit of the output is V^2/Hz.
- A Hamming window with 50% overlap between consecutive windows is applied to reduce spectral leakage.
- The densities are averaged over 10 measurements to increase the signal-to-noise ratio. The results are saved as 338 NetCDF files.

The first 50 Hz of the spectra are not included in the analysis. This is because it contains both unwanted disturbances from pulse tube movement and $1/f$ noise. The spectra are cut off at 10 kHz, because the initial range of the signal is 20 kHz because of the Nyquist, so absolute value of

the Fourier transform only allows the maximum frequency to be half of this value. The PSD of measurement 0 and 200 are shown in Fig. 3.6.

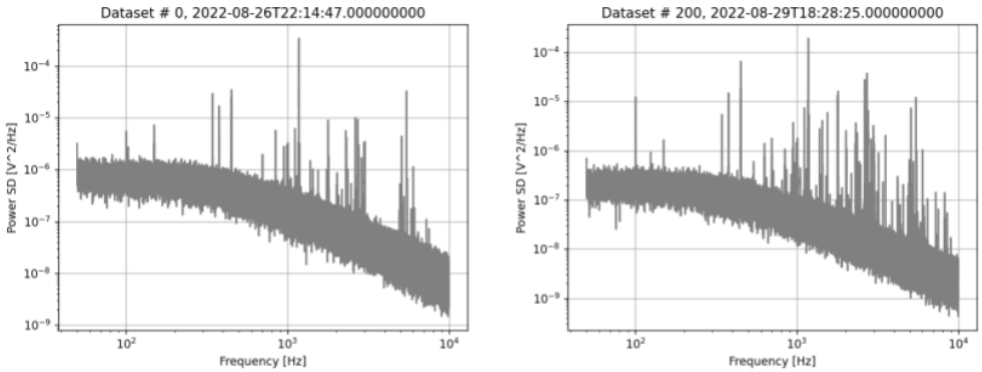

Figure 3.6: *Log-log plot of the PSD* (V^2/Hz) *as a function of the frequency* (Hz) *of data sets 0 and 200.*

The spectra have the shape of a first order low-pass filter with a 3dB point in the order of 10^2 Hz. As can be seen, the data set that corresponds to a later time contains more interference peaks than the first data set. Another thing that is noted is that over time the PSD becomes smaller, indicating that the energy of the spectra will also be smaller.

3.3.1 Removing Interference Peaks

The interference peaks in Fig. 3.6 are caused by multiple external sources. The amount of energy they contain is dependent on their bandwidth. If it is wide enough, it affects the value of the total energy of the noise spectrum in such a way that the accuracy is decreased. It is therefore preferable to reduce the interference in the spectra as much as possible.

The procedure of removing the interference peaks has multiple steps and is applied to all spectra:

- A height threshold of $PSD_{max} = 1.7 \times 10^{-6}\,V^2/Hz$ is set. This is based on the maximum PSD value of the first data set. The data points that are excluded are replaced by a NaN value.
- The data points are divided into 50 Hz bins by selecting the first 305 data sets to process.
- The z-score, which is a measure of how far a point is from the mean in terms of standard deviations, is calculated for each point.

- A z-score threshold of $Z = 6$ is applied to all points (see Fig. 3.7, left). If the z-score is above the threshold, it is replaced by a NaN value.
- The recurrence is defined as the amount of NaN values of all data sets divided by the number of data sets processed, per frequency. This is calculated for all sets, giving an array of values between 0 and 1 for all frequencies.
- A recurrence threshold that changes per frequency is set for all values (see Fig. 3.7, right). For every data set, the points where the recurrence is higher than the threshold are filtered out. The remaining data is labeled as the clean data.

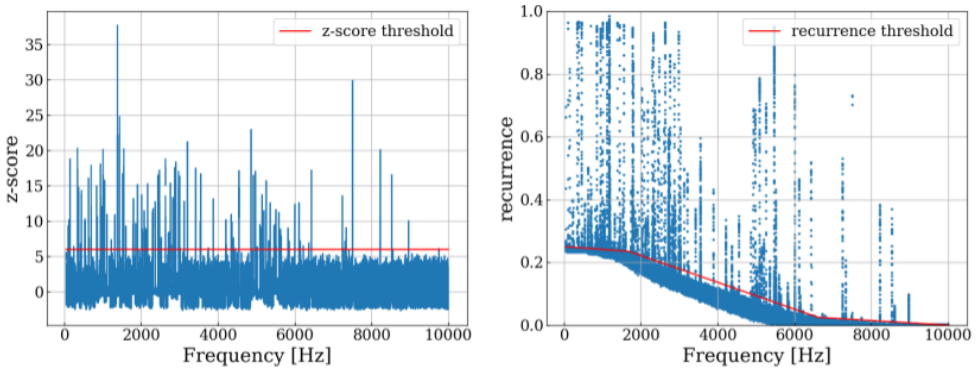

Figure 3.7: Left: *Plot of the z-score per frequency* (Hz) *for data set 200, with the z-score threshold (red).* Right: *Plot of the recurrence per frequency* (Hz) *for all data sets, with the recurrence threshold (red).*

3.3.2 Temperature from Flux Noise

Given that the measurement device is a flux noise thermometer, the point of interest of each data set is the flux noise spectrum. This is found by converting the voltage noise to a flux noise. The conversion factor consists of the gain of the pre-amplifier, which has a value of 10, and a sensitivity of 0.4 V/Φ_0, previously calculated by the Oosterkamp group. After the application of the conversion factor, the result is the magnetic flux noise S_Φ with units Φ_0^2/Hz.

Next, a relation between the flux noise and the thermodynamic temperature is sought. It turns out that the spectral noise power P_Φ is linearly related to T [23]. It can be calculated using Eq. 2.12. In this case, $f_0 = 50\,\text{Hz}$

Version of January 24, 2023– Created January 24, 2023 - 22:30

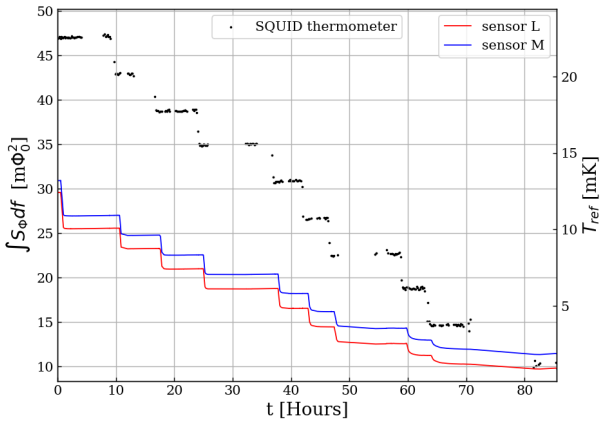

Figure 3.8: *Dual axis plot of the spectral noise power P_Φ (mΦ_0^2) (left) and the resistance thermometer temperatures T_{ref} (mK) (right) over time t (Hours).*

and $f_1 = 10\,\text{kHz}$, the reasons for which have been explained earlier. Since P_Φ is calculated discretely, Eq. 2.12 is replaced by the *numpy.trapz()* function.

Plotting the noise power P_Φ together with the resistance thermometer temperatures gives Fig. 3.8. Clearly, the MFFT and sensors follow the same path, which is an indication that they are measuring the same temperature. Because the units are different however, it does not yet tell us anything about how they compare to each other in terms of accuracy.

To find the slope of the relation $P_\Phi \propto T$, a calibration method that uses the L sensor results as reference temperature is applied. The power P_Φ and reference temperature T_{ref} (mK) are plotted against each other. Given that there are more T_{ref} values than P_Φ values, T_{ref} is averaged over 335 data points. The plot is given in Fig. 3.9.

Next, a linear fit of the data points in Fig. 3.9 that goes through the origin is estimated. Since the resistance thermometer is not necessarily accurate at low temperatures, the fit is done with a reference temperature above 10 mK. Since there are barely any points between 10 and 100 mK, the calibration is done between the 212 and 374 mK, because it displays a set of points that appears most linear out of all other points.

Something to note is that the fit is done to the function $y = ax$, since at zero temperature the spectral power also has to equal zero. The fit is therefore altered in such a way that it forces the best estimation to go through the origin. The error can be determined by means of bootstrapping the chosen data points. While not ideal, given that there are not many data

points used for the fit out of scarcity, it is the most accurate way of finding an error for the MFFT temperatures that result from the calibration.

The calibrated SQUID temperatures can then finally be compared to the resistance thermometer temperatures.

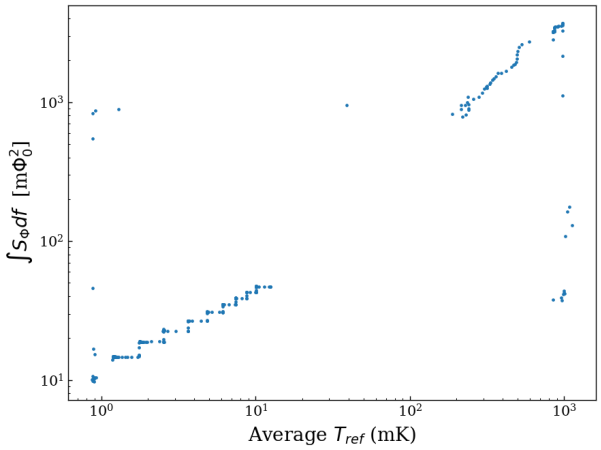

Figure 3.9: *Log-log plot of the power P_Φ (mΦ_0^2) over the averaged T_{ref} (mK).*

Chapter 4

Results and Discussion

The results are centered around the two thermometer types, where the HDL resistance thermometer is discussed first in section 4.1, followed up by the discussion of the MFFT results in section 4.2. The latter section also includes a comparison of the thermometers.

4.1 HDL Resistance Thermometry

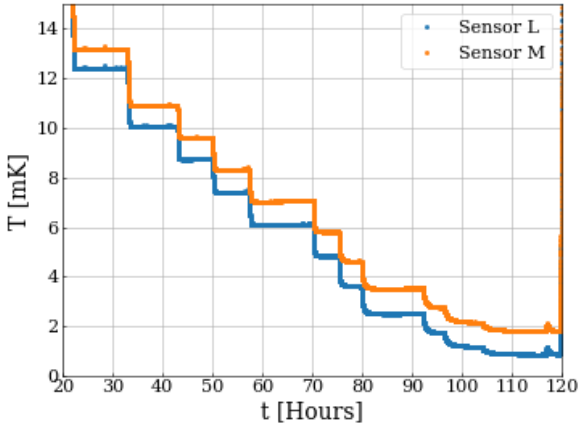

Figure 4.1: *Plot of the temperature T* (mK) *per HDL resistance thermometer sensor over time t* (Hours)*. The M (orange) and L (blue) sensors show the step by step decline of T from 15* mK *to roughly 1* mK *through the NDS.*

The temperatures measured by the sensors are plotted against the elapsed time, shown in Fig. 4.1. The M and L sensors show 11 temperature sweeps

that depict the step by step decrease in the temperature T (mK) achieved through the NDS. In between the sweeps, the temperature stays approximately the same with some fluctuations. In some cases T increases slightly before the next sweep as the system heats up again.

4.1.1 Temperature Fluctuations

Section 3.2 described how the fluctuation of the temperatures in between sweeps could be used to find the temperature mean, which is a way of expressing the temperatures T_M and T_L (mK) of sensors M and L that are reached with each sweep. The corresponding standard deviations serve as estimates of the statistical errors σ_{T_M} and σ_{T_L} of these temperatures. The values can be found in table 4.1. It also shows the temperature difference T_{diff} (mK).

Table 4.1: Table of the temperatures T_M and T_L (mK) of sensors M and L respectively and their difference T_{diff}. The table also shows their corresponding errors σ_{T_M} and σ_{T_L}.

T_L (mK)	σ_{T_L}	T_M (mK)	σ_{T_M}	T_{diff} (mK)
12.93	0.01	13.17	0.01	0.7800
10.06	0.01	10.90	0.01	0.8394
8.746	0.007	9.620	0.007	0.8746
7.415	0.008	8.326	0.008	0.9109
6.11	0.02	7.05	0.02	0.95
4.838	0.004	5.813	0.004	0.9750
3.625	0.002	4.625	0.002	1.000
2.52	0.02	3.52	0.02	1.01
1.754	0.002	2.761	0.002	1.007
1.181	0.003	2.160	0.003	0.9790
0.877	0.006	1.825	0.006	0.9486

The difference between the temperatures of the sensors is apparent in Fig. 4.1. Although they appear to follow the same trend, with their exponential decay curves being identical, there seems to be a difference in the order of 1 mK at all times t (s). Specifically, the mean of the temperature difference is given by $T_{diff} = 0.93 \pm 0.07$ mK. Also notable is that T_{diff} increases at lower temperatures. The cause of this difference and why it increases is due to the fact that the sensors were calibrated with different polynomials. This means that by extrapolating the temperatures outside of the polynomial fit range, you can expect a diverging difference as the

temperatures become increasingly unreliable. The difference in polynomials is the main reason for the difference, but there are more factors that call the reliability of the thermometer into question. The sensors were calibrated in a different setup and then moved to the current one. Since the calibration for such temperatures is specific to the environment and given that the material in the sensors can be easily bent, this further increases the inaccuracy of the thermometer at lower temperatures.

Another thing that can be noted from table 4.1 is the varying standard error of the temperatures, with some standard deviations differing in one order of magnitude from each other. This is attributed to certain time periods in between sweeps having a larger temperature increase than others. The time in which the temperature remains fairly constant is not the same in between every sweep, allowing more time for the system to heat up before the temperature is decreased again. This is also visible in Fig. 4.1. The effect of this is a lower accuracy for some values of T_M and T_L.

Determining whether or not T_L and T_M follow the same trend, which is done in section 4.1.2, is a way of telling how accurate they are compared to each other. This however does not tell us how correct they are in general. To be able to say anything else about the accuracy of the resistance thermometers, they have to be compared to the MFFT. The result of this comparison can be found in section 4.2.2.

4.1.2 RC Time Delay

As mentioned before, the exponential decay curves of the sensors seem identical in Fig. 4.1. By calculating the time constant associated with each curve for both sensors, they can be compared to each other. Fig. 4.2 (left) shows the time constants of the sensors as the time goes on and the temperature decreases. From the left plot it can be observed that for both sensors, τ (s) grows as the temperature T becomes lower with each sweep. This relation is exponential, but is represented with a linear line by using a log-scale for the y-axis. From the best fit estimations it can be determined that $\tau \sim e^{-2T_L}$ and $\tau \sim e^{-4T_M}$ for sensors L and M respectively.

Something that can be pointed out from the figure is that sensor M and L scale differently, while it is expected that they scale in the same way. This assumption is based on the fact that the sensors supposedly work in the same manner and therefore experience the same time delays when measuring. However, considering section 4.1.1, the result is not surprising. The difference in temperature, which increases over time, causes the time constants of the sensors to scale differently. Consequently, if you were

to plot the different τ values using the temperatures of only one sensor, you'd get plots that overlap. The plot for this is shown on the right side of Fig. 4.2.

The fact that τ increases exponentially with T can be attributed to a delay in the heat flow $\dot{Q}$ in the silver wire. The heat flow is dependent on the thermal conductivity κ, which in turn decreases with temperature. This means that for smaller T, it takes longer for the silver wire to achieve the same temperature at points that are further away from the cantilever.

It is important to point out that the difference in the scaling of τ for the two sensors is not caused by the fact that they each measure a different temperature, but because of the aforementioned reason regarding the polynomial fitting. This can be demonstrated by calculating the heat flow between the sensors for a temperature difference of 1 mK, assuming that they are approximate 1 cm apart and the thermal conductivity of silver is $\kappa = 5\,\mathrm{Wcm^{-1}K^{-1}}$. The resulting heat flow is $\dot{Q} = 1\,\mathrm{mJs^{-1}}$. Given that the specific heat of $PrNi_5$, the cooling element, is $C_{PrNi_5} = 1.6\,\mathrm{JK^{-1}}$, the wire would heat up with $0.6\,\mathrm{Ks^{-1}}$. It can be concluded from this that the wire could not stay cold long enough if the temperature difference was due to the sensors measuring a difference, therefore excluding this possibility.

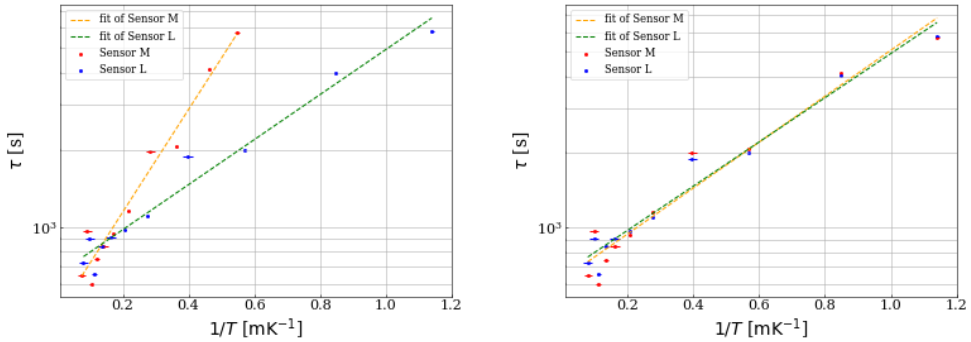

Figure 4.2: Left: *Plot of τ (s) over $1/T$ ($\mathrm{mK^{-1}}$) for sensors M (red) and L (blue), together with the best fit estimations of the data points. The y-axis has a log-scale. The temperature difference between the sensors, caused by incorrect calibration, causes τ to scale differently per sensor.* Right: *The same plot as on the left, but for the case where sensors M and L have the same temperature values.*

4.2 Magnetic Flux Fluctuation Thermometry

4.2.1 Flux Noise Spectra

The temperatures that are measured with a MFFT are based on the flux noise spectra S_Φ (Φ_0^2/Hz), which are dependent on T and vary over the frequency. In Fig. 4.3A, two of these spectra are shown together. The orange colored spectrum corresponds to data set 0 and the blue spectrum to data set 200, where the index of the data set progresses over time. The matching temperatures are lower for data sets with a higher index.

The figure shows that at smaller frequencies the energy in the spectrum is high, but becomes lower at larger frequencies. This is line with what is expected from a low-pass filter. The cutoff frequency of the filter seems to be around 300 Hz.

Another thing that can be seen is that for data sets that correspond to a lower temperature, the flux noise is also lower. Between data sets 0 and 200, S_Φ shrinks with a factor of approximately 4. This is in agreement with Eq. 2.8, where $S_\Phi \propto T$. Finding the value of the constant in this linear relation is left to section 4.2.2.

Furthermore, Fig. 4.3A shows the interference peaks that are present in the noise spectra. Most of the peaks seem to be present in both of the spectra, but blue spectrum contains more peaks. This is because at lower temperatures, the thermal noise in the silver wire is lower, allowing for peaks previously lower than the noise spectrum too become visible. The unwanted noise sources can be electrical equipment among other things. For example, the SQUID feedback and DAQ add a certain amount of noise to the signals that pass through them. At lower noise spectra, these become more obvious.

A second observation that can be made about the interference peaks is that they are higher at larger frequencies. This is because the low-pass filter causes a drop-off of the frequency after the cutoff frequency, making the interference peaks appear higher than at lower frequencies. There is also more interference. These two things can most likely be credited to the noise from DAQ, which processes the signals after an anti-aliasing filter is applied.

The grey peaks in the graphs are the interference peaks that have been removed using the method described in section 3.3. Panels B and C specifically show the separated spectra up to 1 kHz, which gives a better visual of how well peaks are filtered out before the drop-off becomes steep. As can be seen, the filtering process works well for smaller frequencies. This is especially the case for the orange spectrum. The blue spectrum does

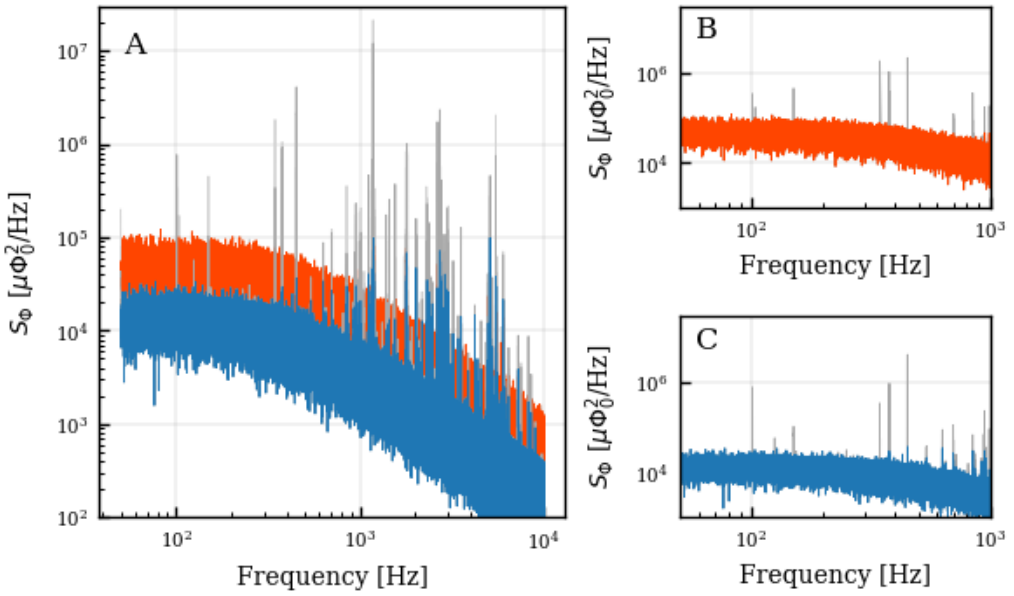

Figure 4.3: Panel A: *Plots of the PSD of the flux noise* S_Φ (Φ_0^2/Hz) *of the MFFT as a function of the frequency* (Hz) *for data sets 0 (orange) and 200 (blue). The frequency ranges between 50* Hz *and 10* kHz. Panels B,C: *The same plots as in panel A, but separated and zoomed between the frequencies 50* Hz *and 1* kHz. *The grey peaks in the graphs are interference peaks that have been filtered out.*

show some inclusion of the interference in the filtered data around the cutoff frequency and above, but the highest peaks in this range have been removed. Looking at larger frequencies (panel A), less interference peaks have been removed. This is amplified at lower temperatures, where a lot of the peaks are still visible in the spectra.

The procedure of removing interference assumes that for every noise spectrum the peaks appear at the same frequencies. Therefore, the filtering mask that was used during the analysis is based on the first data set and subsequently applied to all spectra. The type of interference that was concentrated on stems from electrical noise that is most prevalent at multiples of 50 Hz due to the power grid operating at this frequency. However, it is possible that peaks from this source also appear at other frequencies.

Image plots, or ”waterfall” plots, are a way of showing how well the filtering procedure manages to remove interference. Besides that, it has an added benefit of revealing the size of the bandwidth of the peaks, which indicates how much energy is stored in them. It can therefore convey how necessary it is to remove interference before continuing the analysis.

The plots in Fig. 4.4 and 4.5 are images that assign a flux noise value

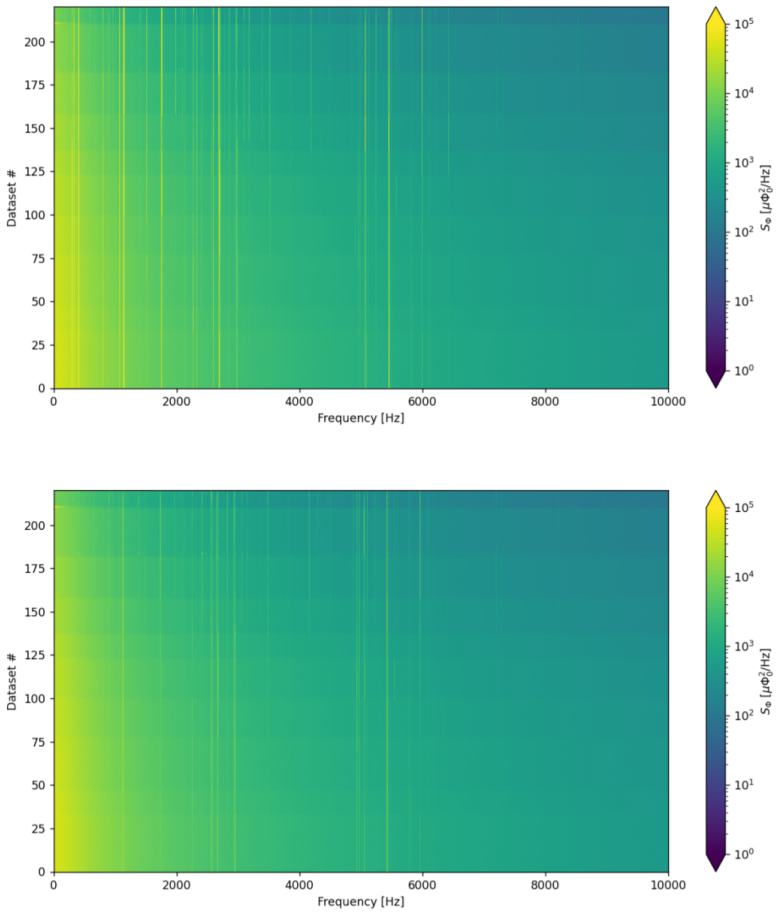

Figure 4.4: *Image plots of the unfiltered (top) and filtered (bottom) flux noise* S_Φ *(*Φ_0^2/Hz*) per frequency (*Hz*) for every data set.*

to each frequency of every data set, where the values are represented by a color from the color spectrum on the right. Fig. 4.4 compares the entire frequency spectrum of the unfiltered (top) and filtered (bottom) data. Visible in the top image is that there are significant interference peaks across all spectra at certain frequencies. They appear a bit above 1 kHz, between 2 and 3 kHz and between 5 and 6 kHz. However, none of these frequencies are distinguishable as originating from a specific source. Their bandwidths are also not especially large compared to the rest of the spectrum. By comparing with the bottom image, it is clear that the filtering works at least partially. While some lines are still visible, they are less distinctive.

Fig. 4.5, which is cut off at 1 kHz, zooms in on the smaller frequencies, where the energy of the spectrum is much higher. Comparing the

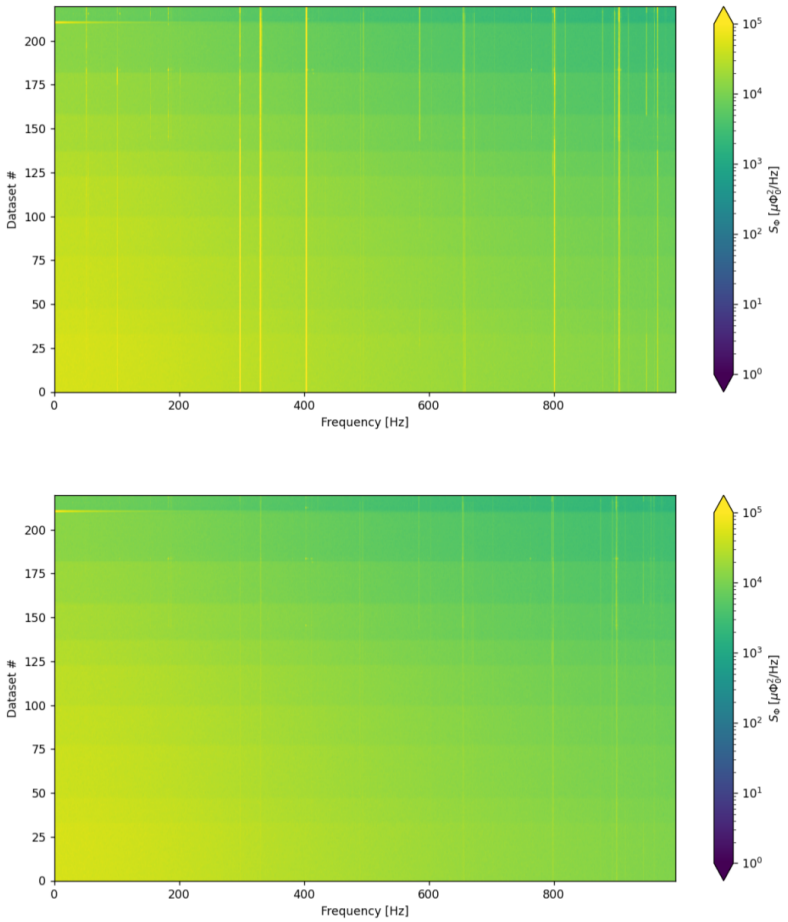

Figure 4.5: *Image plots of the unfiltered (top) and filtered (bottom) flux noise* S_Φ *(*Φ_0^2/Hz*) per frequency (*Hz*) for every data set, zoomed in between 0* Hz *and 1* kHz*.*

unfiltered and filtered images shows that almost all frequently appearing interference peaks have been removed. Hence, it can be concluded from the filtering results that the process works well for frequencies below the drop-off of the low-pass filter.

Something else to notice from the images is that there are blocks where multiple data sets have approximately the same PSD values. The reason for this is that the temperature was decreased bit by bit. Fig. 4.1 and 3.9 show how the temperature is changed in sweeps over time.

Lastly, to know exactly how the filtering affects the rest of the analysis, the noise powers of the filtered and unfiltered spectra are compared to each other in Fig. 4.6. It shows that removing the interference peaks does influence the amount of energy in each spectrum. The filtered line

runs smoother than the unfiltered line, and is consistently lower across the relevant data sets. It can be said that filtering the spectra is a necessary component in processing the MFFT data.

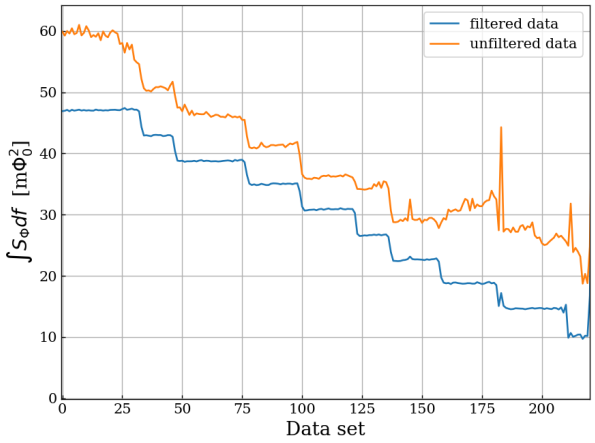

Figure 4.6: *Plot of the noise power P_Φ (mΦ_0^2) per data set for the data that had the interference peaks minimized (blue) and the raw data (orange).*

4.2.2 SQUID Temperatures

Section 3.3 mentions that the data points follow a lienar trend that has a slight negative offset. However, the linear function is forced to go through the origin to satisfy the equipartition theorem. This results in a best fit estimation that has a smaller slope than the data points, as can be seen in Fig. 4.7 (left). The result of this is a less accurate calibration of the MFFT temperatures. The right side of the figure shows that the line goes through the origin, but that it again deviates from the data points. However, since these data points occur below 10 mK, comparing them to the calibration line is at any rate not entirely accurate.

The accuracy of the calibration could be improved if there were more data points to fit with. However, as can also be seen in Fig. 3.9, there is barely any data between 10 and 100 Hz. The reason for this is that after the NDS, the environment was very quickly heated up again, leaving little room for measurements to be done in that time period. This time coincides with the silver wire being in this temperature range, causing the temperature gap.

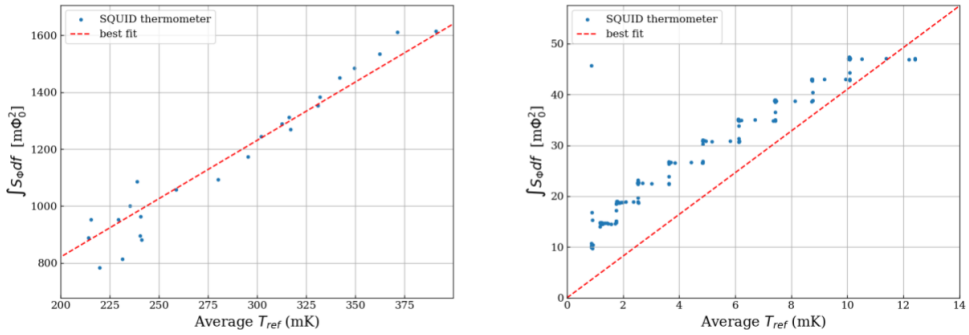

Figure 4.7: Left: *Calibration of the* P_Φ (mΦ_0^2) *data points between* $T_{ref} = 2 \times 10^2$ mK *and* $T_{ref} = 4 \times 10^2$ mK. Right: *Calibration line with respect to* T_{ref} *below 10* mK, *where it is visible that the line goes through the origin.*

The result of the calibration is a slope of $a = 4 \times 10^6$ mΦ_0^2. It is then possible to calculate the SQUID temperature by dividing P_Φ with a, resulting in the plot in Fig. 4.8, which shows how the temperature T of the two different thermometers evolves over time t (Hours).

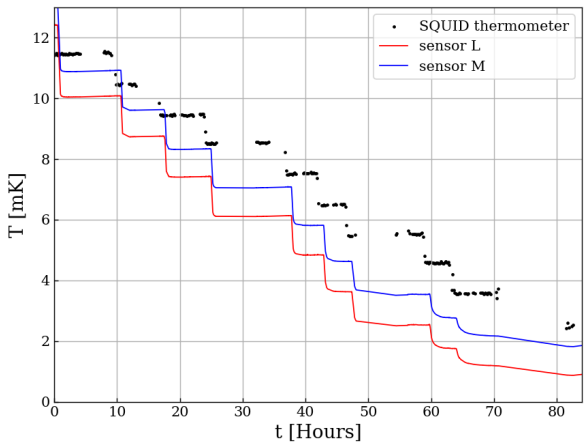

Figure 4.8: *Plot of the temperature* T (mK) *of the MFFT and resistance thermometer over time* t (Hours).

The SQUID temperatures show a notable amount of gaps. This is due to the fact that the MFFT data sets contain a significant amount of time jumps. This can likely be attributed to equipment failure during the measurement period. Besides that, it can be observed that the different thermometers follow the same temperature sweep path, but their tempera-

tures don't line up. In fact, they differ with 1-2 mK. Since the MFFT relies on the thermodynamic temperature, it is more accurate than the HDL resistance thermometer. This implies that the latter does not work perfectly for temperatures lower than 20 mK. However, the error in the calibration of the SQUID temperature has to be taken into account. At around 11 mK, the MFFT aligns the most with one of the sensors (M). Returning to Fig. 4.7, it can be seen that at this temperature the data points and fit function touch. As the temperature decreases from there, the data points and fit line deviate further from each other, which can again be observed in Fig. 4.8. Although the inaccurate fit does not allow for any solid conclusions, it can be assumed that based on this the MFFT and resistance thermometer temperatures would line up with a better calibration. In fact, this is confirmed by previous work of the Oosterkamp group [12].

Chapter 5

Outlook and Conclusion

5.1 Thermometer Accuracy

5.1.1 Comparing Thermometers

Chapter 4 extensively discussed the results of this thesis, which predominantly focuses on the accuracy of the HDL resistance thermometer and the magnetic flux fluctuation thermometer. It is especially considered how exactly they compare to each other, the outcome of this being that at no time do the two thermometers completely line up in temperature. The difference ranges between approximately 1 and 2 mK, which is significant given that the range of interest is in the order of 10 mK. This means that there is at least a 10-20% uncertainty about the measured temperature of the cantilever with these specific results.

There are a few additional things that have to be considered when it comes to how well the thermometers can be trusted. One of them is the fact that the MFFT is a primary thermometer, which makes it inherently more accurate than an externally calibrated resistance thermometer. The aim is to ascertain whether the latter thermometer compares well enough to the MFFT, so that it can be used as the main thermometer instead. This is because it is much easier to perform data analysis for the resistance thermometer due to smaller file sizes and less elaborate voltage to temperature conversions.

Of course, in order to make this step there first needs to be a confirmation that the primary thermometer actually measures the thermodynamic temperature. Run 58 does not verify this because of the uncertainty of the MFFT results, which are affected by two different types of calibration. The first is the calibration of the reference temperature, from sensor L, which

was done with a polynomial fit that becomes increasingly less accurate as the temperature moves further away from the temperature at which the calibration was done. It should also be noted that sensor L was arbitrarily chosen over sensor M as the reference sensor, but given that they have a temperature difference, it cannot be said which one is more accurate. The second calibration is that of the MFFT to the reference temperature, which is done through a forced best fit estimation. This causes the results to not fully match the linear relation between the flux noise and temperature, therefore also contributing to inaccuracy.

To overcome this in upcoming runs, there should be careful consideration for the temperature range that is most optimal for flux noise calibration. Specifically, the calibration should be done at temperatures of known superconducting transitions at which the HDL resistance thermometer is calibrated. In fact, due to the change in environment, it is advisable that the resistance thermometer is re-calibrated in the same dilution fridge as the experiment and MFFT. There should also be plenty of measurements at these temperatures in order to do the most accurate fit.

Finally, it should be remarked that the results of run 56 [12] do show an alignment of the MFFT and resistance thermometer temperatures over time, indicating that the resistance thermometer is most likely a good fit as the main thermometer of the experiment.

5.1.2 Interference Peaks

The removal of the interference peaks of the flux noise power spectral densities turned out to work better for lower frequencies than for higher frequencies. This is a suprising result, given that the filtering method does not necessarily favor certain frequencies. It might stem from the height threshold, which mostly minimizes peaks at the highest part of the spectrum due to it being constant over the frequency. This conclusion suggests that the z-score filtering works less well than intended, and could possibly be altered in the future to work better at higher frequencies.

Naturally, it should be considered how much effect the removal of the interference has on the results. The image plots in section 4.2.1 show that the frequently occuring peaks are lines that are thin compared to the rest of the spectra. However, from the comparison of the filtered and unfiltered flux noise it can be concluded that removing the interference peaks does have a clear positive effect, meaning that even though the peaks are thin, they do hold a fair amount of energy. Besides filtering, it is therefore important to find the cause(s) of the major peaks and effectively eliminate

them.

5.1.3 Thermometer Time Delay

For the resistance thermometer, the time delay was discussed in terms of a time constant, which exponentially scales with the temperature. For a follow-up of this thesis might be interesting calculate the RC time constants according to literature values in order to explain this behaviour properly.

For future experiments,the time delay of the MFFT can also be considered. This could not be examined in run 58 due to there not being enough temperature data points near the exponential curves.

5.2 Towards CSL Measurements

This thesis originally intended to mainly focus on the cantilever measurements of run 60. However, these could not be performed in time because of a few issues with the experimental setup that prevented the silver wire from cooling down to its desired temperature. The first issue is that the silver wire was touching another wire that is thermalized to a a plate above the mixing chamber plate. This happened because as the environment cools down, the material of the wire can deform slightly and move. The second problem was caused by the twisted pair wire going through the 4 K plate. A faulty O-ring caused the OVC and IVC to not be completely sealed off from each other, creating a gas leak. The resulting unwanted thermalization of the plates caused difficulty in the cooling process.

Both of these oversights are easily fixable, so that the next run can most likely implement cantilever measurements with the improved setup.

5.2.1 Improving Upper Bounds

In order to continue setting upper bounds for CSL, it is essential to further improve cryogenic cooling. As previously suggested by Van Heck et al. [12], this may be achieved by implementing another nuclear demagnetization stage. Through this, the cantilever might be further cooled down to temperatures that are consistently below 1 mK. This would make it easier to successfully perform cantilever measurements that can redefine the red colored upper bounds of Vinante et al. [11] in Fig. 2.1 to the black dashed line. Although this is still many orders of magnitudes away from the proposed CSL parameter values of the GRW-model, it is a step in the

right direction to possibly one day measure the effects of CSL and explain measurements at the quantum scale.

Acknowledgements

The results in this thesis were produced in the fall semester of 2022-2023, during which I could almost always be found in the Huygens-Kamerlingh Onnes Laboratory, more commonly referred to as ”de oude meethal”. It was here that I was welcomed into the Oosterkamp group and involved as much as possible in their dynamics and activities, which resulted in a positive and memorable bachelor research period. I would especially like to thank Jaimy for making me feel comfortable enough to ask (many) questions and always finding time to guide me in day-to-day tasks. I also want to thank Tim, Koen, Dennis and Sanaz for creating a fun, interesting and somewhat chaotic work environment that kept me looking forward to continuing the research period. Lastly, I want to thank Tjerk for teaching me how to critically look at results and lending a kind hand whenever necessary.

Bibliography

[1] Menno Poot and Herre S.J. van der Zant. Mechanical systems in the quantum regime. *Physics Reports*, 511(5):273–335, Feb 2012.

[2] Gregg Jaeger. What in the (quantum) world is macroscopic? *American Journal of Physics*, 82(9):896–905, Sep 2014.

[3] Angelo Bassi and Giancarlo Ghirardi. Dynamical reduction models. *Physics Reports*, 379:257–426, Feb 2003.

[4] Paola Cappellaro. 22.51 course notes, chapter 3: Axioms of quantum mechanics. page 15, Oct 2012.

[5] Charlie Wood. Physicists rewrite a quantum rule that clashes with our universe. Oct 2022.

[6] Lautaro Amadei, Hongguang Liu, and Alejandro Perez. Unitarity and information in quantum gravity: A simple example. *Frontiers in Astronomy and Space Sciences*, 8:2, May 2021.

[7] Elias Okon and Daniel Sudarsky. Black holes, information loss and the measurement problem. *Foundations of Physics*, 47(1):120–131, Nov 2016.

[8] Andrea Oldofredi. Some remarks on the mentalistic reformulation of the measurement problem. a reply to s. gao, Jan 2019.

[9] Giancarlo Ghirardi, Philip Pearle, and Alberto Rimini. Markov processes in hilbert space and continuous spontaneous localization of systems of identical particles. *Physical review. A*, 42:78–89, Aug 1990.

[10] Angelo Bassi, Kinjalk Lochan, Seema Satin, Tejinder P. Singh, and Hendrik Ulbricht. Models of wave-function collapse, underlying theories, and experimental tests. *Rev. Mod. Phys.*, 85:471–527, Apr 2013.

[11] A. Vinante, M. Bahrami, A. Bassi, O. Usenko, G. Wijts, and T. H. Oosterkamp. Upper bounds on spontaneous wave-function collapse models using millikelvin-cooled nanocantilevers. *Phys. Rev. Lett.*, 116:090402, Mar 2016.

[12] Bernard van Heck, Tim Fuchs, Jaimy Plugge, Wim A. Bosch, and Tjerk H. Oosterkamp. Magnetic cooling and vibration isolation of a sub-khz mechanical resonator. Aug 2022.

[13] Andrea Smirne and Angelo Bassi. Dissipative continuous spontaneous localization (csl) model. *Scientific Reports*, 5(1):12518, Aug 2015.

[14] Stephen L Adler. Lower and upper bounds on csl parameters from latent image formation and igm heating. *Journal of Physics A: Mathematical and Theoretical*, 40(44):13501, Nov 2007.

[15] Guido van de Stolpe. Global warming through wave function collapse. May 2019.

[16] C. Curceanu, B. C. Hiesmayr, and K. Piscicchia. X-rays help to unfuzzy the concept of measurement. *Journal of Advanced Physics*, 4(3):263–266, Sep 2015.

[17] Sandra Eibenberger, Stefan Gerlich, Markus Arndt, Marcel Mayor, and Jens Tüxen. Matterwave interference of particles selected from a molecular library with masses exceeding 10â000 amu. *Phys. Chem. Chem. Phys.*, 15:14696–14700, Apr 2013.

[18] Stefan Nimmrichter, Klaus Hornberger, Philipp Haslinger, and Markus Arndt. Testing spontaneous localization theories with matter-wave interferometry. *Phys. Rev. A*, 83:043621, Apr 2011.

[19] J. Beyer, Dietmar Drung, A. Kirste, J. Engert, A. Netsch, A. Fleischmann, and C. Enss. A magnetic-field-fluctuation thermometer for the mk range based on squid-magnetometry. *Applied Superconductivity, IEEE Transactions on*, 17:760 – 763, Jun 2007.

[20] Electrical4U. Rl parallel circuit, 2020. Available at https://www.electrical4u.com/rl-parallel-circuit/.

[21] N. Gershenfeld. *The Physics of Information Technology*. Cambridge Series on Information and the Natural Sciences. Cambridge University Press, 2000.

[22] P. Horowitz and W. Hill. *The Art of Electronics*. Cambridge University Press, 2015.

[23] A. Netsch, E. Hassinger, C. Enss, and A. Fleischmann. Novel, non contact noise thermometer for millikelvin temperatures. *AIP Conference Proceedings*, 850(1):1593–1594, Dec 2006.

[24] J. Clarke and A.I. Braginski. *The SQUID Handbook: Fundamentals and Technology of SQUIDs and SQUID Systems*. Wiley, 2006.

[25] G Batey, Andrew Casey, M Cuthbert, Anthony Matthews, John Saunders, and Aya Shibahara. A microkelvin cryogen-free experimental platform with integrated noise thermometry. *New Journal of Physics*, 15, Nov 2013.

[26] M. Palma, D. Maradan, L. Casparis, T.-M. Liu, F. N. M. Froning, and D. M. Zumbühl. Magnetic cooling for microkelvin nanoelectronics on a cryofree platform. *Review of Scientific Instruments*, 88(4):043902, 2017.

[27] Priyanka Jena and Rajesh Gupta. Application of rc delay time for estimation of thermal properties. *Journal of Physics: Conference Series*, 2116(1):012111, Nov 2021.

[28] Adam L. Woodcraft. Recommended values for the thermal conductivity of aluminium of different purities in the cryogenic to room temperature range, and a comparison with copper. *Cryogenics*, 45(9):626–636, Sep 2005.

[29] S Luth and F Pobell. *Matter and Methods at Low Temperatures*. Springer-Verlag, 1996.

[30] ELECTRICAL ENGINEERING. series rc circuit, 2016. Available at https://electronics.stackexchange.com/questions/248882/series-rc-circuit.